

Testing a Novel Method to Map the 3D Distribution of Gas Clouds in Intergalactic Space

by

Daniella C. Bardalez Gagliuffi

Submitted to the Department of Physics
in partial fulfillment of the requirements for the degree of

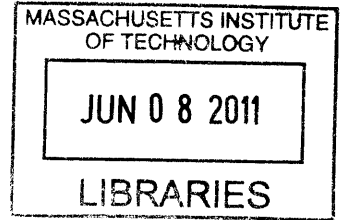
Bachelor of Science in Physics

at the

MASSACHUSETTS INSTITUTE OF TECHNOLOGY

June 2010

© Massachusetts Institute of Technology 2010. All rights reserved.



ARCHIVES

Author

Department of Physics
May 10, 2010

Certified by

Robert Simcoe
Assistant Professor of Physics
Thesis Supervisor

Accepted by

Professor Nergis Mavalvala
Senior Thesis Coordinator, Department of Physics

Testing a Novel Method to Map the 3D Distribution of Gas Clouds in Intergalactic Space

by

Daniella C. Bardalez Gagliuffi

Submitted to the Department of Physics
on May 10, 2010, in partial fulfillment of the
requirements for the degree of
Bachelor of Science in Physics

Abstract

We propose a new method to detect intergalactic Lyman α emitter and absorber systems by comparing broadband and narrowband images. The narrowband observations were carried out with the Maryland-Magellan Tunable Filter (MMTF) at central wavelengths of 5120Å and 5140Å and pointing to the Chandra Deep field South. The broadband images were obtained through the European Southern Observatory public database. Catalogues of galaxies were constructed from all images, taking the R broadband as a reference for locating objects. Via color-color and color-magnitude diagrams, and taking the Steidel et al. color selection criteria as a reference, we were able to identify numerous Ly α emission and absorption candidates. This serves as a proof of concept that narrowband absorption could be used to map the distribution of Lyman limit systems in 3D.

Thesis Supervisor: Robert Simcoe
Title: Assistant Professor of Physics

Acknowledgments

First of all, I would like to thank my parents for feeding my insatiable curiosity and always encouraging me to do my best in everything I do. I wouldn't be the person I am today if it weren't for you.

I am infinitely grateful to my 8.02 and 8.902 professor and thesis advisor, Professor Rob Simcoe, who was always kind to explain concepts to me over and over again and who adopted the unorthodox names I assigned to our figures. Thank you for all the time you spent in helping me to put this thesis together and for making it a smooth process for the most part. More importantly, thank you for sharing your life experiences and thoughtful advice with me. Your mentoring really helped me get through the last very stressful months.

I would like to extend my gratitude to Kathy Cooksey for clarifying all the concepts I didn't understand in Rob's meetings, and for all the technical problems she helped me solve for my thesis. I'm happy I got to spend a semester as your 8.02 TA. I learned so much from you and your genuine desire of teaching. I promise to pass the baton and help someone in need on their thesis sometime along the road.

I would also like to thank all the grad students and professors on the 6th floor of building 37 for creating such a great learning and work environment. Your words of encouragement and undergrad thesis horror stories managed to keep me sane and understand that all this hard work is a rite of passage. In particular, I want to thank Mike Matejek for all the work he put on my MATLAB code, even though in the end we switched to IDL. I would like to thank my friend Melodie Kao for choosing her work desk to be right in front of mine, and being my partner in crime during this year. I absolutely enjoyed all our conversations, scientific and not, and I'm glad we managed to survive together the sweat and tears through the grad school application process and Physics GRE studying.

And last but not least, I would like to thank my boyfriend Joe Poole, and my friends here, there and everywhere for their words of support throughout this year, and especially for putting up with the stressed out Daniella. You were my rock.

I've really enjoyed the exhilarating environment at MIT. Despite the hard work, the

sleepless nights, and the caffeine addiction, I believe these have been the best four years of my life.

Contents

1	Introduction	13
2	Data Reduction and Techniques	19
2.1	MMTF images	19
2.2	ESO images	24
2.3	Image cross-registration	26
3	Analysis	29
4	Discussion and Future Work	41

List of Figures

1-1	Sample LLS composite spectrum in its rest frame	17
1-2	Sample spectrum of a damped Lyman α system.	17
2-1	The IMACS camera and its components.	21
2-2	Sample image taken with a narrowband filter from MMTF.	25
2-3	Sample ESO image taken with the R band filter	27
3-1	Histograms for R, V, and I broadband filters	31
3-2	Color-color diagrams for color selection criteria	33
3-3	Broadband filter location within a sample galaxy spectrum	34
3-4	Color-magnitude diagrams for narrowband colors	36
3-5	Ly α emitters	37
3-6	Ly α absorbers	39

List of Tables

2.1	MMTF Observations	22
2.2	ESO Observations [9]	24
2.3	ESO filter information.	24
3.1	Magnitude and color information about the selected galaxies in figures 3-5 and 3-6	38

Chapter 1

Introduction

Surveys of the intergalactic medium (IGM) have been previously done using spectra of quasars (very bright active galactic nuclei (AGN) powered by the accretion disk of the black hole at their center). However, these represent only a small percentage of the total galaxy population (AGN fraction is between 0.1-3% at low redshifts [8]). In addition, obtaining spectra from quasars only allows us to study the IGM in one dimension. Moreover, quasar spectra has the disadvantage of being more expensive in terms of telescope time than galaxy spectra. In contrast, it would be much more efficient to survey gas clouds by using galaxies, given that they are more numerous, since we can find hundreds of galaxies per quasar. On the other hand, the challenge presented by galaxies is their intrinsic faintness compared to quasars, especially when taking spectra, and the fact that the ones we want to study are located at large distances.

We are experimenting with a novel method to map IGM clouds in three dimensions using narrowband imaging of galaxies instead of quasar spectroscopy. Using a variety of broadband and narrowband filters, it should be possible to construct a catalogue of IGM clouds through discrete slices in redshift by comparing the images.

The field we have chosen is the Chandra Deep Field South (CDF-S) which covers an area of 0.11 deg^2 . This is the most studied field in the sky as it was probed by Chandra X-Ray Observatory Survey [7], Hubble Ultra-Deep Field [3], Great Observatories Origins

Deep Survey (GOODS) [6] and other prior redshift surveys.

Public imaging data in the optical range from the European Southern Observatory (ESO) taken with broadband filters were used for this thesis project, in combination with images from the Magellan Telescopes, using the Maryland-Magellan Tunable Filter (MMTF) at narrowband widths. The innovative technique used in this project will allow us to observe absorption line features at a higher contrast than we would by just using broad filters.

The first step of the analysis is to calibrate the photometric measurements coming from the different instruments and filters, and register the images to each other. Then we will identify the galaxies that will be used as background sources from examining the broadband images. After that, we select those and measure their color against narrow band MMTF images. We will find that some galaxies drop out of the narrow filters, and that is due to IGM clouds absorbing radiation at that particular wavelength. Moreover, some galaxies will appear especially bright in the narrowband filters and this can be attributed to Lyman α emission lines. In this way, we can assemble a catalog of “drop-out” and emission galaxies for each redshift we have available.

The IGM represents 95% of the total baryonic matter of the universe [14]. Even though these clouds have very low densities, they still occupy a large volume. We are interested in mapping the distribution of IGM clouds, drop-out and emission galaxies. This will provide insight to answer deeper questions about galaxy formation as the conclusions we would draw from a random IGM distribution or a physical correlation between IGM clouds and the nearby galaxies will differ significantly.

The intergalactic matter, as its name suggests, is the matter filling the largely void spaces between galaxies. It is a low density gas primarily composed of Hydrogen and Helium, but it can contain traces of metals as they are expelled from the galaxies via supernovae. The constituting gas of the IGM is highly ionized, having a neutral Hydrogen fraction of $\frac{n_{HI}}{n_H} < 10^{-4}$ [13] as compared to the total Hydrogen available (ionized plus neutral). This high ionization also contributes to the IGM’s considerably high temperature of 3×10^4 K [13].

The ionization of the IGM occurs due to the high frequency light coming from O and

B stars, AGNs, and quasars. All these sources are energetic enough such as to produce photons with at least 13.6 eV, capable of ionizing Hydrogen. This energy corresponds to a wavelength of 912 Å, which falls in the ultraviolet regime of the electromagnetic spectrum. When the ionized IGM recombines back into neutral Hydrogen, it emits a Lyman α photon.

The Lyman α line in neutral Hydrogen spectrum corresponds to the electronic transition from $n = 2$ to $n = 1$, which gives rise to the emission of a photon of wavelength $\lambda = 1215.67\text{\AA}$. However, Ly α emission photons coming from distant galaxies and quasars, suffer from significant redshift on their way to the Earth due to the expansion of the universe, such that they become observable in the optical regime.

Some of the most common sources of astrophysical Ly α are gas clouds surrounding O and B stars, which are among the most massive types of stars and consequently the ones with the shortest lives. The larger the initial mass used in forming a star, the shorter its life will be. A new-born massive star needs a high rate of Hydrogen fusion in its interior in order to achieve enough pressure to prevent it from a subsequent gravitational collapse. In this way, the star will run out of fuel more quickly than a lower mass star and eventually undergo supernova to start the same cycle again. These types of stars are also the brightest, so they have the ability of producing energetic photons in the UV, capable of ionizing the surrounding the interstellar medium (ISM), thus emitting Ly α . Therefore, a Lyman α line in a galactic spectrum is usually related to the instantaneous star formation rate [10].

For the case of AGNs and quasars, there is a black hole at the center with an accretion disk around it. As matter spirals into the black hole and is accelerated in its way to the center, it is heated through viscous accretion and emits blackbody radiation in the UV. The light emitted in this scenario is sufficiently energetic to ionize the neutral Hydrogen near the central engine, and thus we observe Ly α [10]. This is consistent with observations of highly ionized Hydrogen in the surroundings of quasars and AGNs. [13].

Since the IGM has such low density and does not produce light of its own, the only way to detect it through the absorption signature it leaves in quasar spectra. The Lyman α forest is a series of absorption lines from neutral Hydrogen which are ubiquitous in quasar and high

redshift galactic spectra. Despite the high degree of ionization in the IGM, the volume that these photons have to cross in order to reach the Earth is so great that the probability of finding a neutral Hydrogen atom to ionize is quite large. This is the reason why we observe a “forest” of lines instead of a single absorption line. This particular distribution of spectral lines shone light on the filamentary structure of the IGM.

Observationally, the Lyman absorber systems can be classified according to the column density of the IGM. The lowest column density clouds $N_{HI} \sim 10^{14} \text{ cm}^{-2}$ give rise to the Lyman α forest. As we go higher in column density, we observe Lyman limit systems and damped Lyman α systems.

Lyman limit systems (LLS) are absorption line systems with column densities $N_{HI} > 10^{17} \text{ cm}^{-2}$. LLS are optically thick to Hydrogen ionizing photons. These systems show an absorption line at $\lambda_{abs} = 1216 \times (1 + z_{sys}) \text{ \AA}$, where z_{sys} is the redshift of the LLS [15]. In addition, there is a “blackout” (absence of lines/significant decrease of flux) blue-ward of the rest frame wavelength of $\lambda_{min} = 912 \text{ \AA}$, since a photon needs to have at least a wavelength of 912 \AA to ionize Hydrogen. Figure 1-1 shows a composite quasar spectrum with marks on important spectral lines.

Another important type of Lyman systems are the damped Lyman α (DLA) systems, which are very strong absorbers with column densities of $N_{HI} \gtrsim 10^{20} \text{ cm}^{-2}$ [15]. On the spectrum, the DLAs have very distinctive “wings” as they can be seen in figure 1-2.

In the next section we will describe the techniques used for the reduction of the narrow-band and broadband images utilized in this thesis. In section §3, we explain the method followed for obtaining catalogues of galaxies from the images and examining their colors in order to classify them into Ly α absorbers or emitters. Section §4 discusses the results and explores applications of this method which can be useful for future work. Finally, a summary and motivation of the work done is presented.

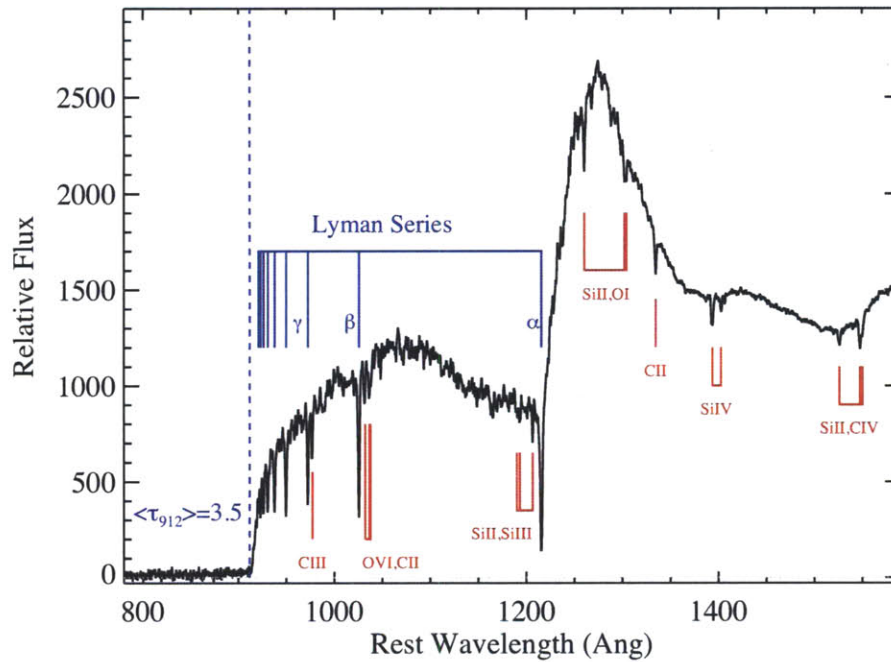


Figure 1-1: Sample LLS composite spectrum in its rest frame. Up to a wavelength of 912\AA , we can see the blackout. The Lyman series begins at the Lyman break, and the Lyman α absorption line is deep at 1216\AA . Source: [12]

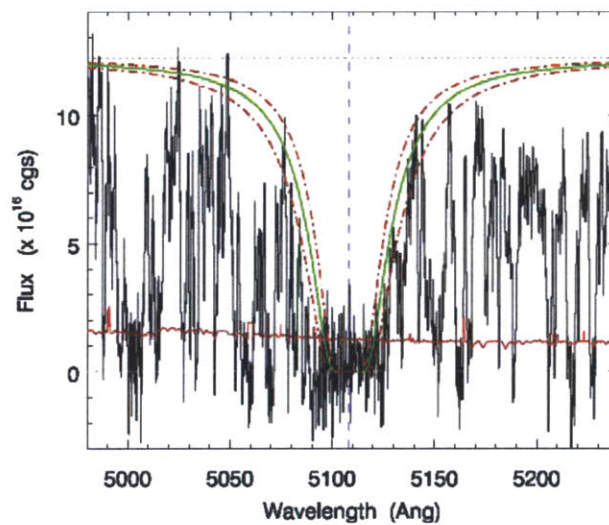


Figure 1-2: Spectrum of a damped Ly α system at $z = 3.202$. The best fit solutions indicate the density of this cloud is $N_{HI} = 10^{20.65} \text{ cm}^{-2}$. Source: [11]

Chapter 2

Data Reduction and Techniques

Our data were taken in the direction of the Chandra Deep Field South (CDF-S) which is centered at RA=3:32:28.0 , Dec=-27:48:30 (J2000), in the constellation *Fornax*, in the Southern Hemisphere. It is 16' across, covering 0.11 deg² of sky [7]. This region has been thoroughly studied in the X-ray, as it was chosen to be part of an ultra deep survey with the Chandra X-Ray Observatory, particularly because of the low occurrence of dust and gas from the Milky Way in that direction.

For this thesis, the CDF-S was observed with the Magellan Baade Telescope at two narrowband filters, and compared to public broad band data from the European Southern Observatory 2.2m Telescope. In this section, we explain the instruments involved in observations and the data reduction pipeline.

2.1 MMTF images

The Maryland-Magellan Tunable Filter (MMTF) is a tunable narrowband imaging filter designed for the Inamori Magellan Aerial Camera and Spectrograph (IMACS) at the Magellan Baade 6.5m Telescope, located at Las Campanas Observatory, Chile. Tunable filters are particularly useful for distinguishing faint signals from the noise coming from the sky [19], such as Lyman α emission line signatures.

IMACS is a wide-field imager whose transmitting spherical collimator, shown in figure 2-1, produces a 24' diameter field of view and a slightly vignetted 30' diameter field [5]. The short camera's field of view is spanned by 8 chips and has a 8192×8192 CCD array and a 0.2 "/pixel plate scale.

The MMTF is a Fabry-Perot type filter composed of two parallel glass plates with high reflectivity surfaces, separated by an air gap. The system is known as an etalon. The width of the gap ranges between 5Å and 15Å [19]. By adjusting piezo-electric stages, the central wavelength of the filter can vary from 5000Å to 9200Å.

The filter has a varying transmission function due to the interference of light rays between the plates. When a light ray enters the etalon it can pass through the second plate or it can be reflected from it. The phase difference after reflection should equal a multiple integer of the wavelength, such that there can be constructive interference at the detector. Equation 2.1 explains how constructive interference is achieved by fixing the path travelled by the reflected ray to a wavelength change of phase of 2π . In this equation, d is the spacing between the plates, m is a non-zero positive integer called the "order number" and λ_T is the wavelength of the transmitted light.

$$2dm = 2\pi\lambda \Rightarrow \lambda_T = \frac{md}{\pi} \quad (2.1)$$

Since $1 < m < \infty$, the transmission function will look like a series of sharp peaks at the λ values corresponding to m 's. The effect of changing the size of the gap is to change the spacing between the m 's in the transmission curve, thus allowing for a wider selection of narrowband filters in a single apparatus. Additionally, a broad band filter whose range includes the narrowband filter of interest, must be placed in the detector such that it blocks the transmission from the unwanted order numbers.

Due to the geometry of the filter, the interference pattern forms in the gap between the plates. Specific wavelengths are imaged according to their radial distance from the optical axis, i.e. the axis traversing the center of the plates. Incoming rays along the optical axis will be mapped near the center of the CCD, while those rays coming off-axis (and thus

traveling a distance $d\cos\theta$ across the plates instead of simply d , where θ is the off-axis angle) will be mapped at a radial distance which correlates to the incidence angle. As a result, the wavelength will vary slightly from the center of the CCD, going outwards. Higher order interference must be eliminated in order to minimize the variation of wavelength and obtain nearly monochromatic images.

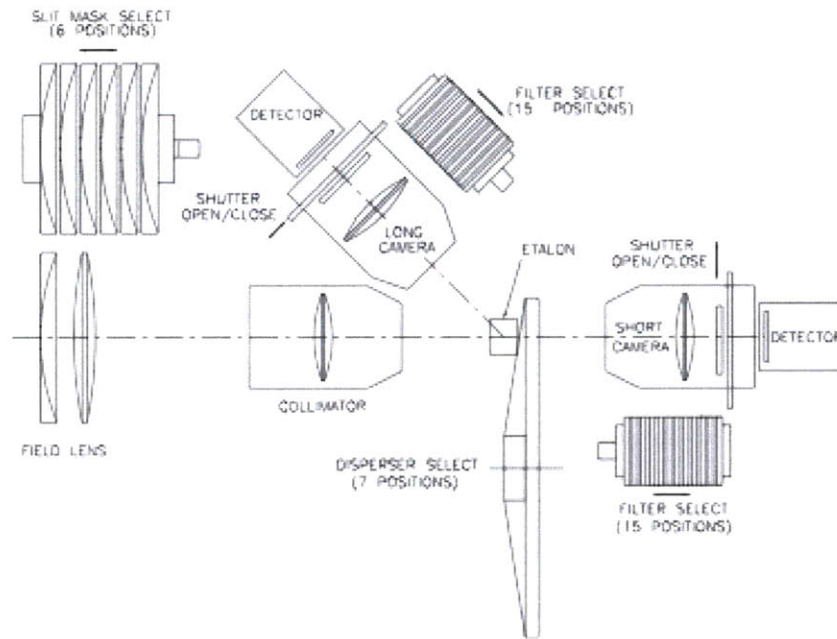


Figure 2-1: Schematic of IMACS camera and MMTF filter. Light comes from the left, crosses the field lens, gets focused by the collimator and then enters the etalon (MMTF). Filtered light then goes to the short camera, crosses another filter and ends up in the detector. [19]

The observations were carried out during observing runs on December 2007 and October 2008, with narrowband filters centered at 5120\AA and 5140\AA to the Chandra Deep Field South region by Prof. Rob Simcoe (MIT) and Ben Weiner (U. Arizona). Therefore, the field was imaged at redshifts of $z = 3.211$ and $z = 3.227$, respectively. More detailed information about the observations can be found in table 2.1.

Table 2.1: MMTF Observations

Filter name	Observation date	Exposure time	Seeing	Number of stacked images
5120	30OCT2008	1500 s	0.605	17
5140	14DEC2007	1800 s	0.712	27

MMTF image calibration

The standard MMTF data reduction pipeline can be found at <http://www.astro.umd.edu/~veilleux/mmtf/datared.html>.

For any image calibration pipeline, the basic frames used are bias, flat fields and dark frames. Bias are zero-second exposures taken with the shutter closed. These measure the electronic zero-point offset which is intentionally added to the CCD counts. Flat fields are images taken with the shutter open pointed at a homogeneously illuminated area, such as the dome of the observatory or a part of the sky during astronomical twilight. These images show the relative sensitivity of each pixel to photons. Darks are images taken with the shutter closed for the same duration as the science frames, which estimate the thermal motion of electrons on the CCD. Dark frames are not required for image calibration if data is taken from large telescopes, such as the Magellan, since these have efficient cooling systems which render dark current negligible. Bias and flat fields, however, are always required.

The first steps toward data reduction were bias subtraction and flat fielding. Bias and flats were combined into a masterbias and a masterflat. Flats were normalized to unity with respect to the image’s central region. Bias were subtracted from all images and bias-corrected science images were divided by the bias-corrected flat fields, as shown in equation 2.2:

$$Final\ image = \frac{S - Z}{F - Z} \quad (2.2)$$

where S is science image, Z is bias (or zero) frame, and F is flat field.

The next step was cosmic ray and bad pixels masking. Traditional methods of cosmic ray detection are based on the contrast between bad pixels and their surroundings, but occasionally the cosmic rays are larger than the point spread functions (PSF) used to model

stars and galaxies, and they may get overlooked. Instead, a more robust method to identify cosmic rays in an image is the Laplacian Edge detection routine for IRAF (LA Cosmic) developed by Pieter van Dokkum [18]. The routine convolves the image with the Laplacian of a Gaussian function, thus matching the zero-crossings (points where the Laplacian changes sign) of the image and the Laplacian. The standard deviation is used to determine the smoothness of the edge. Occasionally, there will be cosmic rays left unmasked after LA Cosmic. However, it would be rare for LA Cosmic to miss a cosmic ray completely. Therefore, with a cosmic ray detected but poorly masked, one can apply an IRAF task (*crgrow*) in order to expand the mask by a single pixel in every direction.

The sky was azimuthally averaged (averaged over equal radii rings) given the mapping correspondence of CCD pixels to focal plane and the location of the optical axis. Subsequently, astrometry solutions were required to join the 8 chips composing the CCD. Since the IMACS camera has a small f-ratio and hence a wide field of view, the mapping of field of view to sky is nonlinear at large field angles. The higher order polynomial terms of these solutions are known *a priori* from crowded star field observations taken by the MMTF instrument team. An absolute WCS was obtained by matching the catalogued positions of known US Naval Observatory (USNO) stars to image position on the focal plane. These offsets, calculated on a frame-by-frame basis, were used to register the multiple exposures into a single, deep composite for each setting of the etalon.

Using the astrometric solutions, the chips were combined into a multi-extension FITS file (MEF). In a similar fashion, all the bad pixel maps were combined into a single one per exposure. Consequently, a stellar catalogue was obtained. This catalogue excluded stars farther than 3500 pixels from the center and with magnitudes outside the range $10 < mag < 19$ [19].

Model PSF catalogues were matched to the stellar catalogue in order to obtain a mode seeing value, which was inserted into the header. With this information, frames were degraded to match the one with the largest seeing. Finally, frames were stacked in two groups with central wavelengths 5120 Å and 5140 Å settings of filters. A sample reduced FITS

frame is shown in figure 2-2.

2.2 ESO images

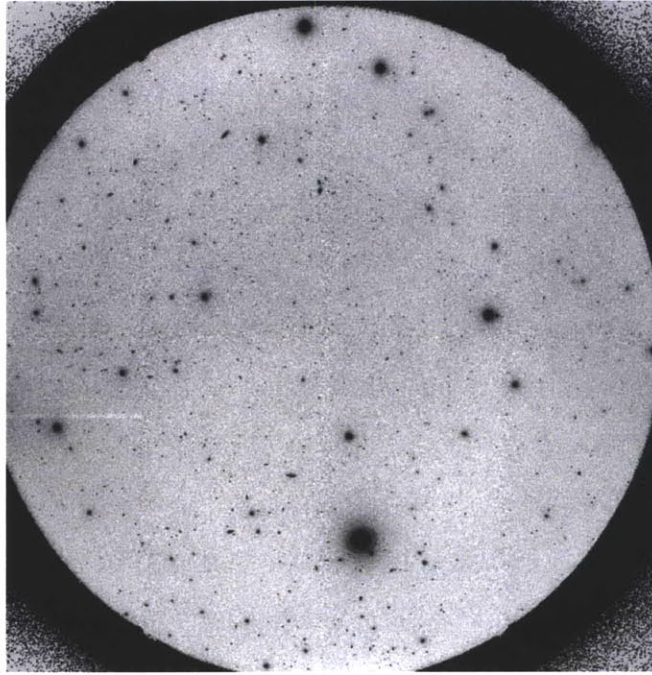
Broadband images of the CDF-S were taken at the MPG/ESO 2.2m Telescope and the ESO New Technology Telescope (NTT) at the La Silla Observatory in La Serena, Chile, under Program-ID No. 164.O-0561 with the Wide Field Imager (WFI) camera [1]. The WFI camera has a field of view of $33' \times 34'$ and a pixel scale of $0.24''/\text{pixel}$ [2]. These images were used for background subtraction and to select high-redshift objects. Fully calibrated and reduced images in UBVRI filters from CDF-S were downloaded from the European Southern Observatory public database. More information about the images and the filters can be found in tables 2.2 and 2.3, respectively.

Table 2.2: ESO Observations [9]

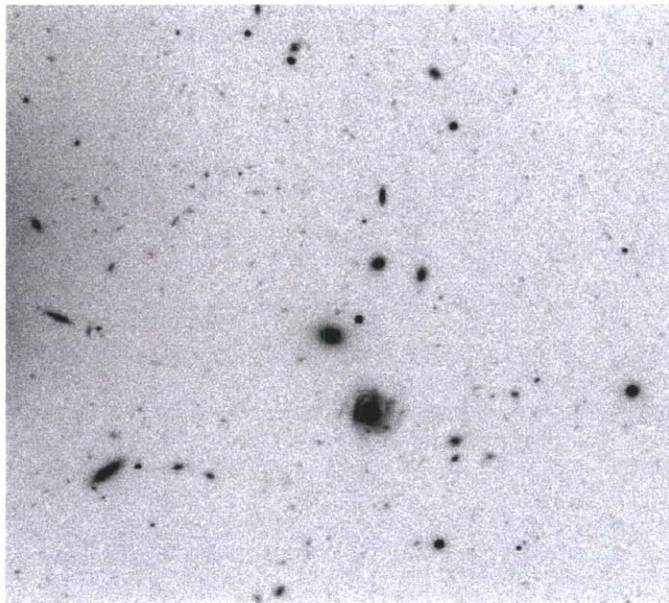
Filter name	Observation date	Exposure time	Seeing	Limiting magnitude	# Stacked images
U	26OCT2000	47595.50 s	0.98	–	55
B	26OCT2000	24546.85 s	1.02	–	30
V	26OCT2000	9247.29 s	0.97	27.75	33
R	26OCT2000	9247.30 s	0.86	25.5	33
I	05NOV1999	26926.40 s	0.93	26.75	46

Table 2.3: Central wavelength and full width at half maximum of ESO filters. * The transmission function of the I filter depends on the response of the CCD, therefore the value is only approximate. [9]

Filter	Central Wavelength	Width
U38	3636.90 Å	382.6 Å
B99	4562.52 Å	990.14 Å
V/89	5395.62 Å	893.86 Å
Rc/162	6517.25 Å	1621.84 Å
Ic/Iwp	7838.45 Å	~400 Å*



(a) $A \sim 0.14 \text{ deg}^2$



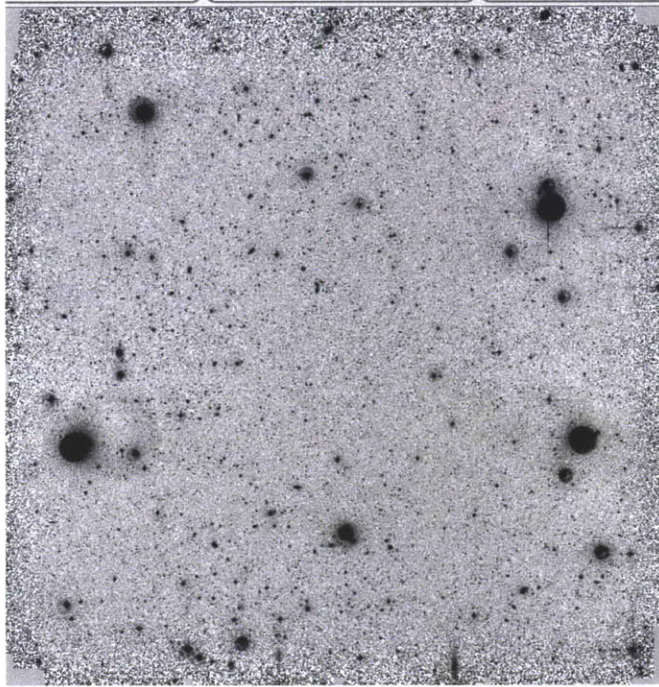
(b) $A \sim 2 \times 10^{-4} \text{ deg}^2$

Figure 2-2: Combined image for 5120Å filter. Figure 2-2(a) shows the entire field of view of the IMACS camera and figure 2-2(b) is a zoomed-in region. The number of galaxies in an area about a thousandth of the original suggest the large depth of the image. Areas are approximate.

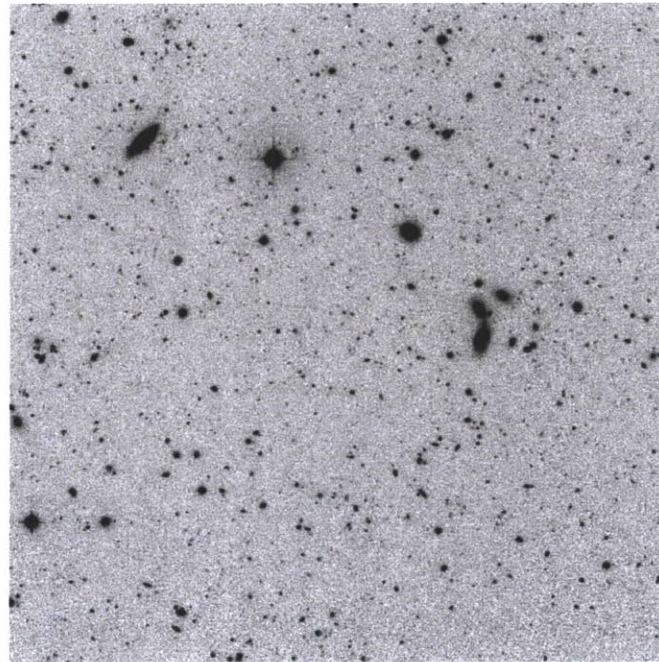
2.3 Image cross-registration

A catalogue of star positions in right ascension and declination was obtained from the MMTF images using IRAF. These coordinates were then transformed to pixel positions in x and y and accurately centered on the stars. The same procedure was applied to the ESO frames. However, while the ESO images had a square field of view, the MMTF images were circular. Therefore, the star catalogues found from ESO were constrained to only include stars within the circumference of the MMTF frames, such that the catalogues would match.

To register the ESO images with respect to the MMTF frames properly, an IRAF routine was applied to find solutions for the transformation of the coordinate systems such that both (x,y) positions on the images and world coordinates would match. The reference image for the transformations was the ESO R filter. This choice was made because selection of high redshift galaxy candidates is usually defined with respect to R [16]. Finally, the solutions were applied and the new registered images generated. Figure 2-3 shows a sample registered ESO image.



(a) $A \sim 0.31 \text{ deg}^2$



(b) $A \sim 9 \times 10^{-4} \text{ deg}^2$

Figure 2-3: Figure 2-3(a) shows the entire field of view in the R filter and figure 2-3(b) is a zoomed-in cut-out region. Areas are approximate.

Chapter 3

Analysis

Our analysis consisted of extracting magnitudes in broadband and narrowband images and comparing them to find Ly α emitters and dropouts. For this end, we used the industry-standard Source Extractor software to perform photometry.

Source Extractor is a robust software which can identify and analyze galactic sources directly from the image. First, SExtractor tries to estimate the value of the sky background by subdividing the image into smaller grids and estimating the local sky background. Then, it takes the sky values from all the smaller grids and combines them around their median.

The object detection is done by convolving a point spread function with the section of the image in question. This method is called “thresholding” and does not distinguish between stars and galaxies until the end. This method works remarkably well with low surface brightness objects, as compared to peak detection, which is more accurate for stars.

Given the abundance of low surface brightness objects, it is indeed likely that two or more may appear blended. In that case, a multiple isophotal analysis technique is performed by which the connected pixels are thresholded again at exponentially spaced brightness levels (i.e. thresholded at different magnitudes). From this, the objects will be separated if their integrated pixel intensity is greater than a determined fraction of the total intensity of the blended objects.

After all detections have been made and deblended, it is important to filter them since

false positives are usually found around very faint objects. The way to solve this problem is by trying to prove that even if the surroundings had been clean, the detection would have still been made. The contribution of the suspected false detection to the mean surface brightness of the neighbors is calculated and subtracted from the mean. If the brightness of the object falls above the surface brightness threshold, then the object is accepted into the catalogue.

SExtractor also calculates the total magnitude of all objects in the catalogue. The method used was adaptive aperture photometry, which consists in taking an elliptical aperture, approximately equivalent to two isophotal “radii”, and calculating its first moment, i.e. its expectation value. No correction was applied to the initial magnitude results. [4]

The ESO image in the R band was used as a reference for finding objects and defining isophotal apertures. Magnitudes in other bands were extracted using identical apertures for calculating colors. For this end, we ran SExtractor first on the R band image only and were able to build a catalogue from the objects in this filter. Using the vector association function (ASSOC_VECTOR), we were then able to run SExtractor simultaneously on two images with the R band catalogue for source detection and a second image in a different filter for measuring magnitudes. The program ran through the R band catalogue to define the (x,y) coordinates of each galaxy, then found the same objects in the second image. After performing photometry on the galaxies from the second image, SExtractor compiled a single catalogue of objects appearing in both images and its corresponding magnitudes. In the case that SExtractor was not able to match an object from the R catalogue to the second image (probably because the object was not bright enough in that filter), it gave a magnitude of 99, clearly indicating an error. This same procedure was applied for the combinations of R and V band, R and I band, R and 5140Å, and R and 5120Å. The raw number of galaxies found through this routine exceeded 130,000.

Figure 3-1 are histograms of source counts for the R, V, and I filters for objects detected in R. The peak from V magnitude is not shown, but it reaches ~ 27.75 mag. The peak in the histograms indicates the detection limit at each filter. As we can see more clearly in figure 3-1(a), the drop in number of galaxies happens after ~ 25.5 mag. SExtractor still

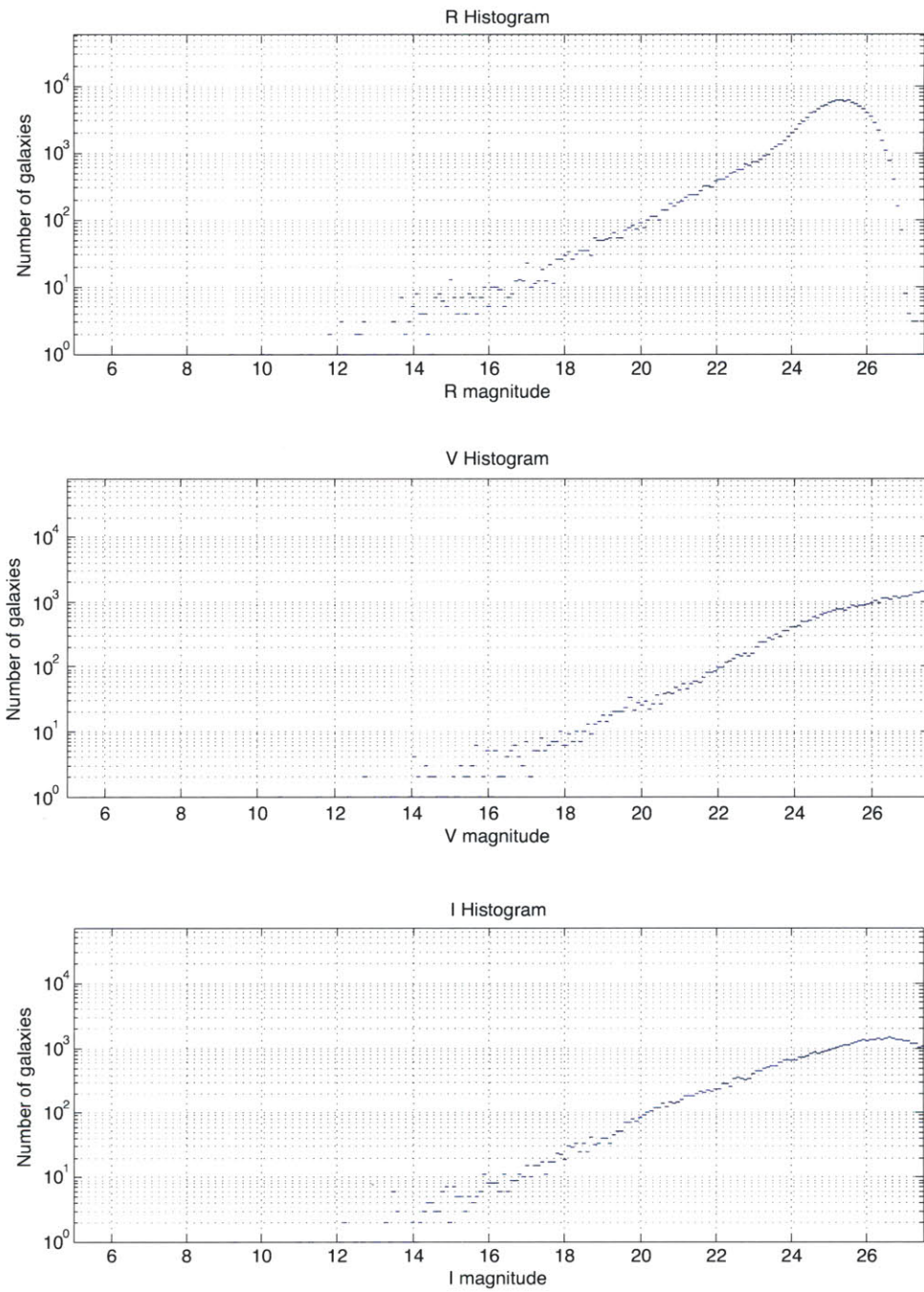


Figure 3-1: Histograms for the three broadband filters used to determine the color selection criteria. The peak determines the limiting magnitude of the filter, therefore, it gives us an idea of reliability from the colors we may be detecting.

gave us magnitude values beyond the detection limits, so these plots are very important to distinguish between real detections and false positives. The scatter at low magnitudes is due simply to the lower occurrence of bright nearby galaxies.

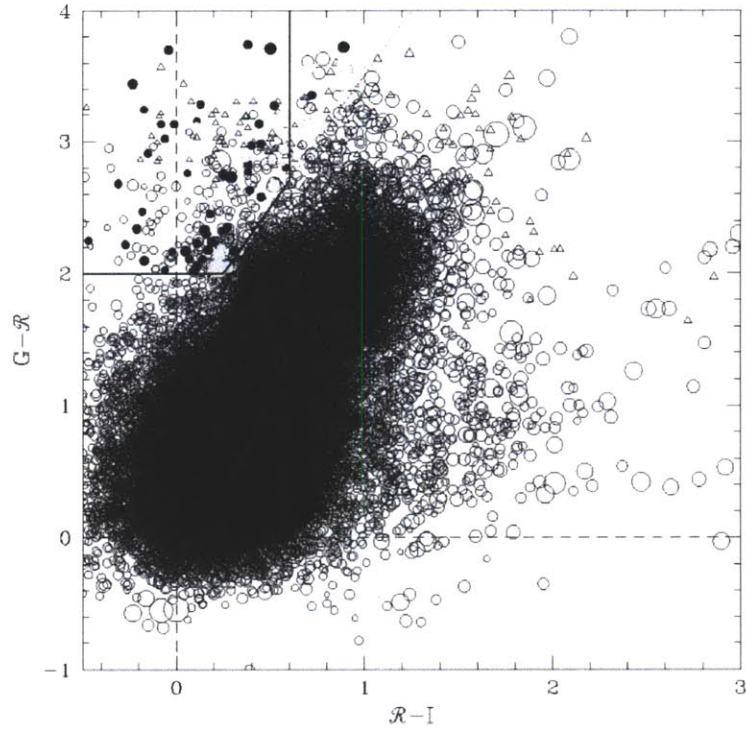
Steidel et al. explains a method to select high redshift galaxies from a color-color diagram. Their analysis uses G, \mathcal{R} and I filters. The G filter has a central wavelength of 4830Å, which is $\sim 565\text{\AA}$ bluer than the V filter used in this study ($\text{CWL}_V = 5395\text{\AA}$). The \mathcal{R} filter was specifically designed for the Steidel et al. analysis to be an intermediate filter between R and I, centered at 6930Å. As a reference, R and I filters have central wavelengths of 6517Å and 7838Å, as previously shown in table 2.3.

Colors are computed by subtracting magnitudes. Equation 3.1 describes how magnitudes and colors are calculated, where F_R is the flux in R and F_I is the flux in I.

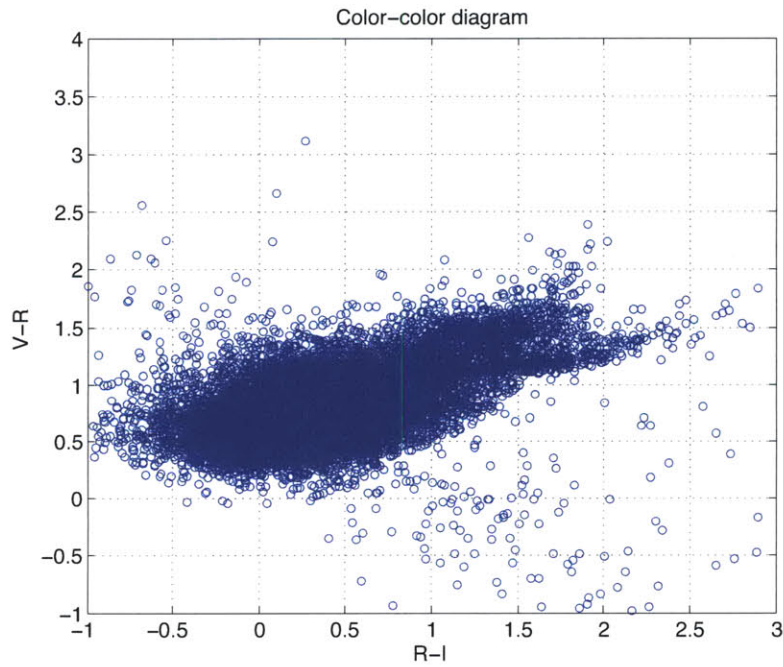
$$R - I = -2.5 \log_{10}\left(\frac{F_R}{F_I}\right) \quad (3.1)$$

Galaxies bluer on \mathcal{R} -I and simultaneously redder on G- \mathcal{R} were candidates for high redshift galaxies according to Steidel et al. Bluer color of \mathcal{R} -I indicates a stronger flux coming from \mathcal{R} filter than I filter and similarly, a redder color in G-I suggest a stronger flux coming from the I than from the G filter. As we go higher in redshift, the galaxy spectrum, as the one shown in figure 3-3, shifts to the right towards longer wavelengths. Making the parallel between their G and our V filters, their \mathcal{R} and our R, and the I filters, this means that the Lyman α emission line will move across our V filter, eventually leaving it to enter the R filter regime. Therefore, as the spectrum becomes brighter in R than in V, the V-R color becomes positive and increasing with redshift. This is the reason why the selection window for high redshift galaxies in Steidel et al. and in our study, corresponds to the top left of the color-color diagram shown in figure ??.

It is worth noting the slight difference in filters when comparing figures 3-2(a) and 3-2(b). Since their \mathcal{R} filter is a compromise between R and I, the \mathcal{R} -I color appears bluer in their diagram since the \mathcal{R} and I filters are closer together, whereas R-I in our study looks redder given the larger wavelength spacing between the filters.



(a) Steidel et al. color selection criteria.



(b) Color-color diagram of galaxies found in CDF-S.

Figure 3-2: Color-color diagrams as determined by Steidel et al. and our study. The central wavelength of the filters used in both cases changes slightly, and therefore so does the general shape of the dispersion plot. High redshift galaxies are shown in the upper left.

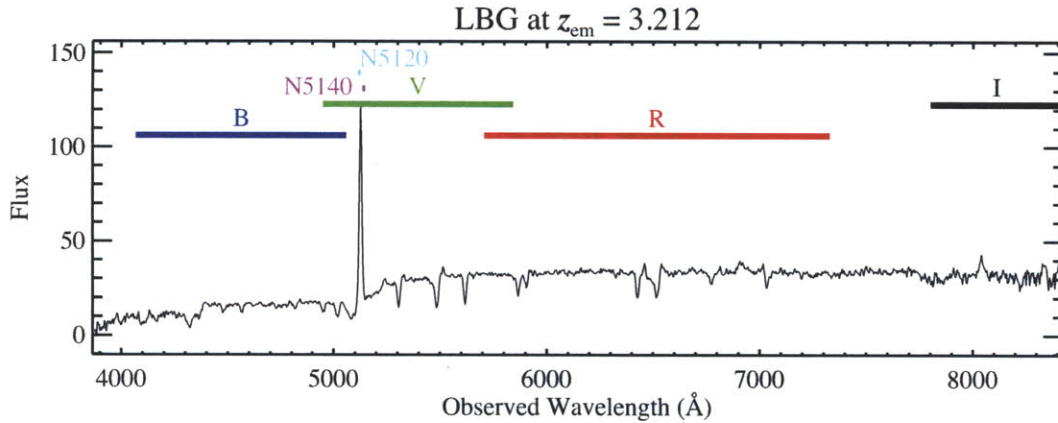


Figure 3-3: Sample galaxy spectrum with BVRI and narrow bands 5120Å and 5140Å. Figure credit: Kathy Cooksey.

Figure 3-3 shows a sample galactic spectrum at redshift $z = 3.211$ and the wavelengths along which the broadband filters lie. It is clear in this plot to see the Lyman α emission line and how the narrowband filters relate to the line. The Lyman α forest are the absorption lines to the left of the emission line, and the part of the spectrum to the right of the Ly α line is due to stellar light. The U filter lies too far left, so it does not appear in the sample spectrum anymore.

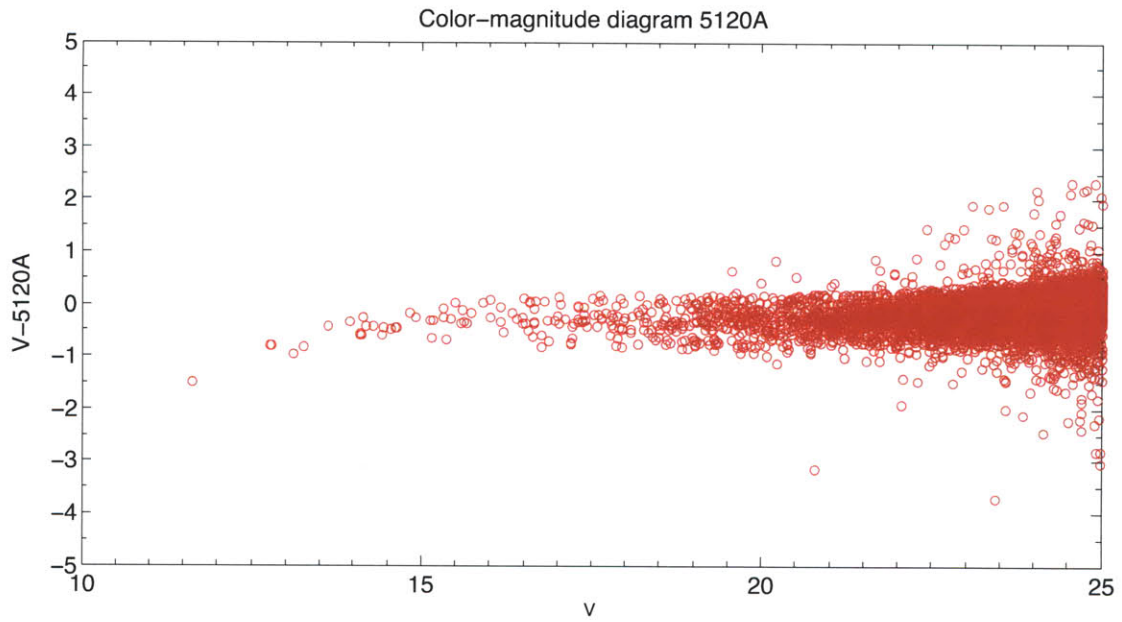
Since both narrowband filters, 5120Å and 5140Å, are contained within the V filter, they are useful to detect sharp features in the galactic spectra. Figures 3-4(b) and 3-4(a) are color-magnitude diagrams which give information about these sharp features within the V filter.

As we can see in figure 3-4, galaxies are centered around zero V-5140Å color, meaning that most of them have a magnitude in the narrowband approximately equal to that in the wide band, thus showing no outstanding features in their spectra. Those galaxies lying above the zero V-5140Å color line show more flux in the narrowband than in the wide band, which indicates the presence of a Lyman α emission line. These galaxies are particularly interesting since Lyman α emission is a sign of a star formation region. Conversely, the galaxies lying below the zero V-5140Å color line show less flux in the narrowband than in

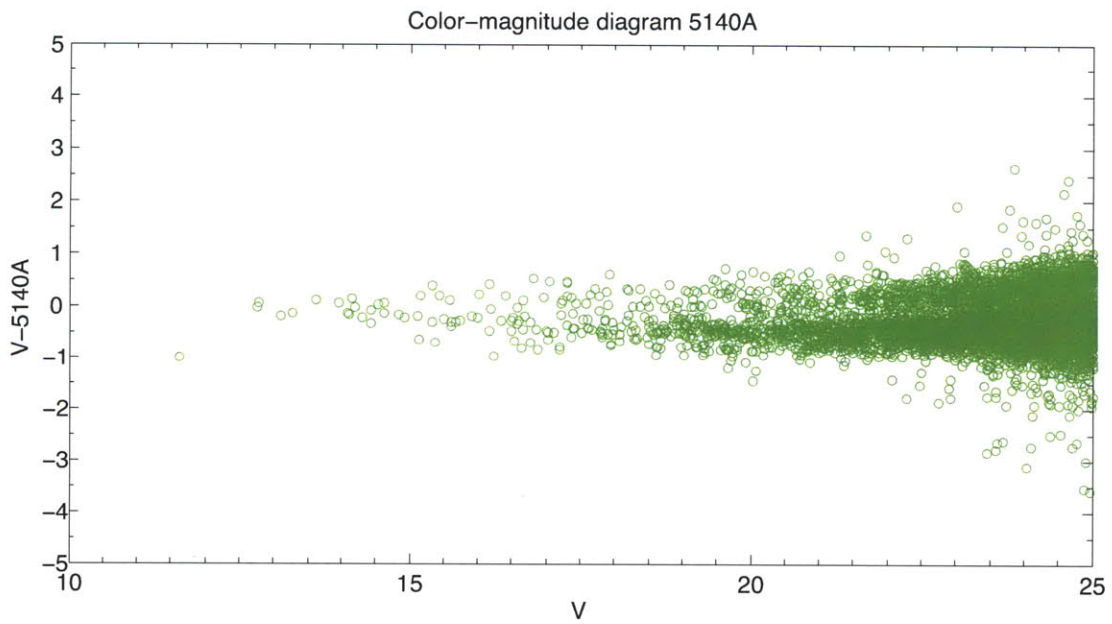
the V band, which indicates the narrowband filter falls on the Lyman limit system region of the spectrum, denoting these galaxies as Ly α absorbers. This further indicates the presence of a cloud of intergalactic matter between the absorption galaxy and us.

We selected galaxies with a $V - 5120\text{\AA}$ or $V - 5140\text{\AA}$ colors to be greater than 1 or less than -1 , so as to admit Lyman α emitter systems and Lyman α absorbers, respectively. From a sample of 1000 galaxies, we chose the 10 emitters and absorbers which seemed more interesting. Figure 3-5 shows an example of 5 emitter systems, located at the center of each frame. The frames are organized by filter, where R, V, I are the first three in that order, followed by 5120\AA and 5140\AA . Figure 3-5(a) shows a galaxy visible in R and V, quite faint in I and especially bright in 5140\AA . In the next figure, 3-5(b), we can see a galaxy in the R and V filters located at the center, again fainter in I and brighter in 5140\AA . In addition, there are two galaxies in the lower right of the 5140\AA frame that are barely visible in all other filters. Therefore, we have found 3 Lyman α emitter candidates in one frame. In figure 3-5(c), the galaxy is very faint in all three broadband filters, and becomes very bright on 5120\AA . Figure 3-5(d) show a galaxy brighter in 5140\AA than in the V filter. It is possible that this candidate is an AGN given that it looks like a point source. Finally, figure 3-5(e) appears to be very faint in V and I filters, and then its brightness spikes at 5120\AA .

For the case of the absorber systems, figure 3-6(a) shows a faint galaxy in the center of the R magnitude frame, which is brighter in V and I filters, but then completely disappears at 5120\AA and remains very faint at 5140\AA . This suggests an absorption line at 5120\AA . Figure 3-6(b) is centered around the upper right galaxy in the quadruple system. It is possible that this image may be only one gravitationally lensed galaxy. The top two galaxies, while bright in R, V, and I filters, get fainter in 5120\AA and the one in the right almost completely disappears in 5140\AA . Figure 3-6(c) is centered about the lower galaxy from the center pair, and we can see it dropping out of the 5120\AA frame. Figure 3-6(d) shows a galaxy in all broadband filters which then disappears in 5120\AA and appears fainter in 5140\AA . Paying closer attention to 5140\AA , we see a candidate for a Lyman α “blob”, which are enormous (~ 100 kpc) Lyman α emitter gas clouds only seen at high redshifts. This kind of objects spark interest because



(a) 5120



(b) 5140

Figure 3-4: Color-magnitude diagrams for narrowband colors at 5120Å (figure 3-4(a)) and 5140Å (figure 3-4(b)). The spread in the data increases as we go higher in V magnitude, due to the intrinsic faintness of higher redshift galaxies, and thus lower signal-to-noise ratio.

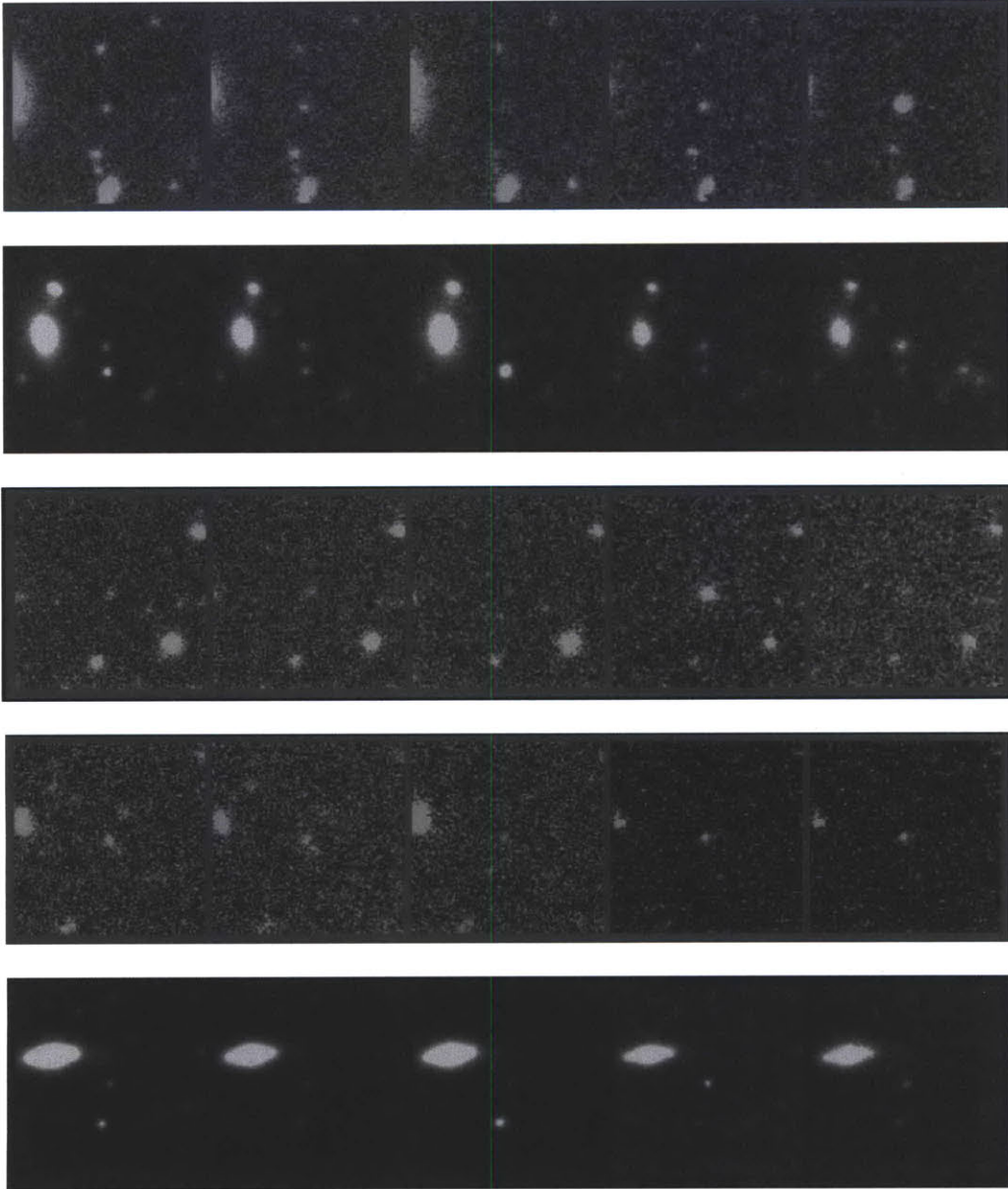


Figure 3-5: Ly α emitters

they have been very little studied, as they were only discovered in 2000 by Steidel et al. [17]. The mechanism for the emission is unknown. Finally, figure 3-6(e) shows a galaxy which seems to be a LLS in 5120Å and another galaxy on top and to the right of the central one, which does not appear in any of the broadband filters, possible due to intrinsic faintness, but it appears very bright on the 5140Å filter thus indicating that it is a Ly α emitter.

Table 3.1 provides information about the magnitude of the galaxies in each filter and the two narrowband colors from the selected galaxies.

Table 3.1: Magnitude and color information about the selected galaxies in figures 3-5 and 3-6

Lyman system	V mag	V - 5120Å	V - 5140Å
	25.12	0.73	1.83
	24.61	0.89	0.77
Emitters	27.08	2.56	-0.02
	25.70	0.91	1.42
	24.80	1.56	0.66
	24.68	-1.09	-0.14
	24.80	-0.39	-2.00
Absorbers	24.39	-1.17	-0.53
	25.45	-1.40	-0.52
	23.93	-1.03	-0.66

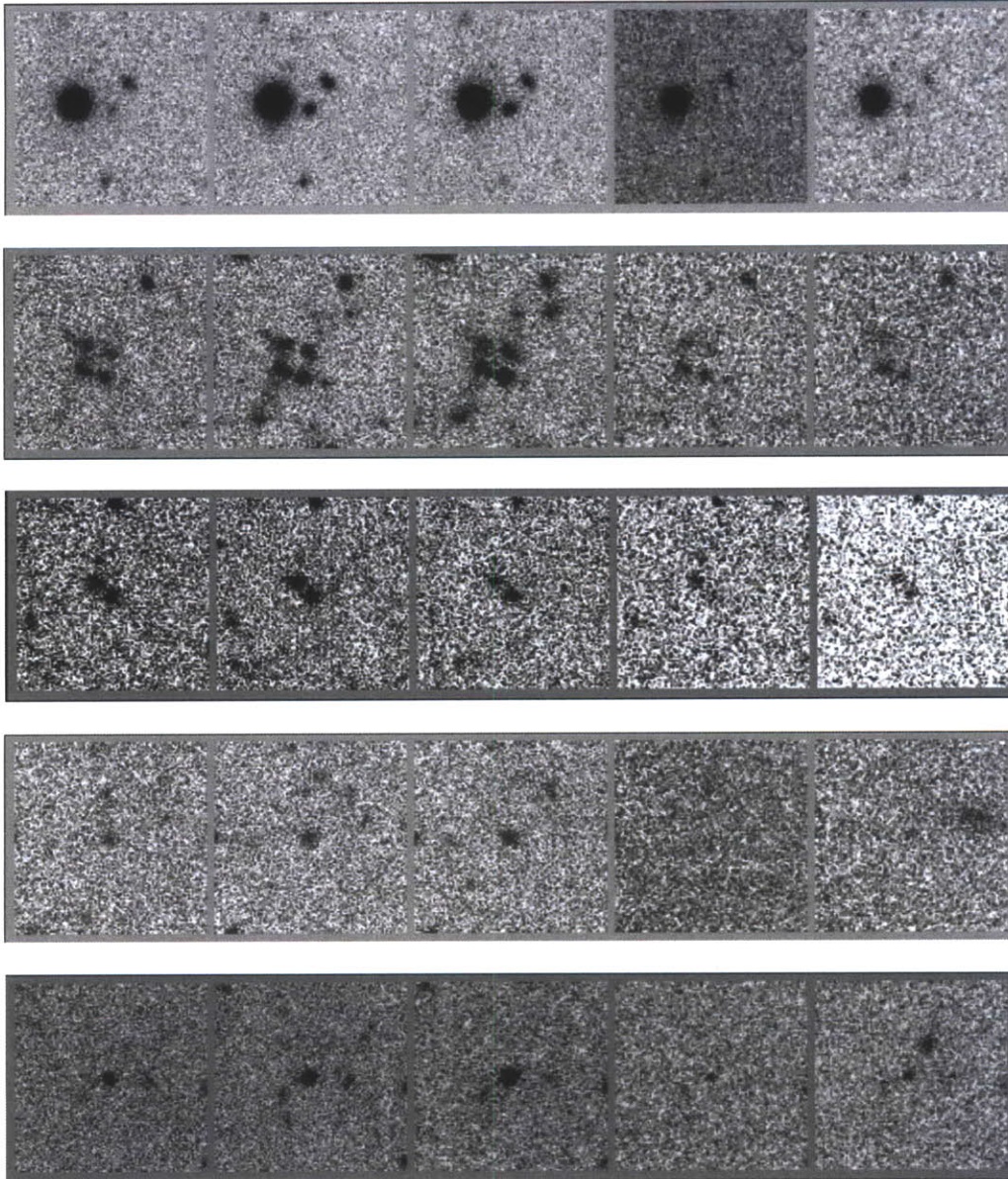


Figure 3-6: Ly α absorbers

Chapter 4

Discussion and Future Work

The IGM is mostly unexplored territory. The fact that IGM clouds can only be observed through absorption on the spectra from background objects, adds difficulty to its study. However, these clouds are very important since understanding them will take us a step further towards understanding how galaxies form.

With this thesis, we tried to find emission and absorption systems in a different way than using quasar spectroscopy. From our search we have successfully found Lyman α emitter and absorber candidates. Further tests are needed in order to confirm that the absorber systems are in fact Lyman α , and not another transition from a lower redshift galaxy, like OII for example (Rest wavelength: $\lambda_{OII} = 3727\text{\AA}$). The spectrum of a galaxy, as that in figure 1-1, shifts to the right as the redshift grows. The possibility remains that the excess brightness in the narrowband as compared to the broadband filters, could signify a different emission line at a slightly different redshift.

It is not possible to study the low-density Lyman α forest with our filter set because the equivalent width of the forest spectral lines is too small, and even our narrowband filters are too wide for that case. As we can see in equation 4.1, since the rest frame equivalent width is in the order of 0.1\AA , this value multiplied by the redshift of our galaxies, yields numbers still in the order of 10^{-1} which are two orders of magnitude smaller than the width of our narrowband filters $\sim 15\text{\AA}$ (Simcoe, personal communication). Therefore, there would not

be enough contrast between the depth of the absorption line and the total flux coming into the filter. We would need narrower filter, in the order of $\sim 1\text{\AA}$ or less.

However, for the case of Lyman limit systems, this method proves to be viable. The equivalent width of absorption lines from an LLS goes from 1 to a few Angstroms. As seen in equation 4.2, if we take for example an equivalent width of 3\AA we find that when redshifted to $z = 3.2$, it will be about 9.9\AA wide. As opposed to the Lyman α forest case, this width is comparable to the width of our narrowband filters, and therefore medium density LLS become detectable with our approach.

$$\omega_{Ly\ \alpha\ forest} \sim 0.1\text{\AA} \times (1 + 3.2) \sim 0.4\text{\AA} \quad (4.1)$$

$$\omega_{LLS} \sim 3\text{\AA} \times (1 + 3.2) \sim 9.9\text{\AA} \quad (4.2)$$

Our knowledge of Lyman limit systems is limited. It is important to know the dimension of Lyman α emission and absorption systems as well as their rate of occurrence, since these factors would lead us to have a better grasp on problems related to galaxy formation.

We would also want to find absorption systems where the gas halo of a foreground galaxy absorbs the light coming from a background quasar. Observationally, both galaxy and quasar would appear close to each other in a broad band image, but only the galaxy would be visible in the narrowband image, assuming the narrowband filter includes the wavelength of the Ly α absorption line. In this way, the light coming from the background quasar, on its way to the Earth, will travel across large volumes of diffuse IGM (which give rise to the Ly α forest) and eventually go through a galactic gas halo (shown as a Lyman α absorption line in the spectra). The occurrence of this type of systems will shine light on the location of galaxies within the IGM filaments.

If this method becomes automated, then it would have the potential of becoming a powerful tool for detecting Lyman α systems. For this thesis we managed to do the absolutely necessary to prove the method. However, in the time allotted it was not possible to try to improve it. There is still an important personal component when selecting candidate galaxies.

Summary

We proved that it is possible to use broadband and narrowband images to detect Lyman absorption and emission systems. This is a fundamentally different methodology from quasar spectroscopy, which has been done for decades. By using galaxies rather than quasars, we get hundreds of samples per field, rather than only a few.

Narrowband images and broadband images from the Chandra Deep Field South were compared in order to see contrast between these in such a way that the higher or lower brightness in the narrowband filters, as compared to the broadband, would indicate the detection of a Lyman emission or absorption system, respectively. The narrowband images were taken with the MMTF at central wavelengths of 5120Å and 5140Å. The broadband images were obtained from the European Southern Observatory in UBVRI filters, although ultimately we only used VRI.

The images were registered to each other, taking the R band as a reference. Once the coordinates were matched, we proceeded to use SExtractor, a standard software which produces a catalogue of galaxies based on the images alone. SExtractor yielded more than 130000 galaxies. From these we excluded all the ones which appeared to have a magnitude beyond the detection limit.

Examining the broadband colors we found a galaxy distribution similar to that of Steidel et al. [16]. The narrowband colors helped us further select the possible Lyman α emitter and absorber candidates. Those galaxies which looked brighter in the narrowband than in the broadband were Lyman α emitter candidates, whereas the galaxies visible in the broadband, but significantly fainter in the narrowband were Lyman α absorbers.

In conclusion, our narrowband imaging method has given its first positive results, since we were successfully able to identify Lyman α candidates by comparing the narrowband to the broadband images. This forms the basis for followup spectroscopy to confirm the method. More work remains to be done with the details of target selection, but this shows that narrowband imaging is a viable way to map absorption systems over large fields of view.

Bibliography

- [1] S. Arnouts, B. Vandame, C. Benoist, M. A. T. Groenewegen, L. da Costa, M. Schirmer, R. P. Mignani, R. Slijkhuis, E. Hatziminaoglou, R. Hook, R. Madejsky, C. Rit e, and A. Wicenec. ESO imaging survey. Deep public survey: Multi-color optical data for the Chandra Deep Field South. *A&A*, 379:740–754, November 2001.
- [2] D. Baade, K. Meisenheimer, O. Iwert, J. Alonso, T. Augusteijn, J. Beletic, H. Belle-mann, W. Benesch, A. B ohm, H. B ohnhardt, J. Brewer, S. Deiries, B. Delabre, R. Donaldson, C. Dupuy, P. Franke, R. Gerdes, A. Gilliotte, B. Grimm, N. Haddad, G. Hess, G. Ihle, R. Klein, R. Lenzen, J.-L. Lizon, D. Mancini, N. M unch, A. Pizarro, P. Prado, G. Rahmer, J. Reyes, F. Richardson, E. Robledo, F. Sanchez, A. Silber, P. Sinclaire, R. Wackermann, and S. Zaggia. The Wide Field Imager at the 2.2-m MPG/ESO telescope: first views with a 67-million-facette eye. *The Messenger*, 95:15–16, March 1999.
- [3] S. V. W. Beckwith, M. Stiavelli, A. M. Koekemoer, J. A. R. Caldwell, H. C. Ferguson, R. Hook, R. A. Lucas, L. E. Bergeron, M. Corbin, S. Jogee, N. Panagia, M. Robberto, P. Royle, R. S. Somerville, and M. Sosey. The Hubble Ultra Deep Field. *AJ*, 132:1729–1755, November 2006.
- [4] E. Bertin and S. Arnouts. SExtractor: Software for source extraction. *A&AS*, 117:393–404, June 1996.
- [5] B. C. Bigelow, A. M. Dressler, S. A. Sheckman, and H. W. Epps. IMACS: the multiobject spectrograph and imager for the Magellan I telescope. In S. D’Odorico, editor, *Society of Photo-Optical Instrumentation Engineers (SPIE) Conference Series*, volume 3355 of *Society of Photo-Optical Instrumentation Engineers (SPIE) Conference Series*, pages 225–231, July 1998.
- [6] M. Dickinson, M. Giavalisco, and GOODS Team. The Great Observatories Origins Deep Survey. In R. Bender & A. Renzini, editor, *The Mass of Galaxies at Low and High Redshift*, pages 324–+, 2003.
- [7] R. Giacconi, P. Rosati, P. Tozzi, M. Nonino, G. Hasinger, C. Norman, J. Bergeron, S. Borgani, R. Gilli, R. Gilmozzi, and W. Zheng. First Results from the X-Ray and Optical Survey of the Chandra Deep Field South. *ApJ*, 551:624–634, April 2001.

- [8] D. Haggard, P. J. Green, S. F. Anderson, A. Constantin, T. L. Aldcroft, D.-W. Kim, and W. A. Barkhouse. The Field X-ray AGN Fraction to $z = 0.7$ from the Chandra Multiwavelength Project and the Sloan Digital Sky Survey. *ApJ*, 723:1447–1468, November 2010.
- [9] Larry Manmaker. *The Wide-Field Imager Handbook*. European Southern Observatory, May 2005. This is a full MANUAL entry.
- [10] Kim K. Nilsson. *The Ly α Emission Line as a Cosmological Tool*. PhD thesis, Københavns Universitet, 2007.
- [11] J. X. Prochaska, S. Castro, and S. G. Djorgovski. New Damped Ly α Metallicities from Echellette Spectrograph and Imager Spectroscopy of Five Palomar Sky Survey Quasars. *ApJS*, 148:317–326, October 2003.
- [12] J. X. Prochaska, J. M. O’Meara, and G. Worseck. A Definitive Survey for Lyman Limit Systems at $z \sim 3.5$ with the Sloan Digital Sky Survey. *ApJ*, 718:392–416, July 2010.
- [13] M. Rauch. The Lyman Alpha Forest in the Spectra of QSOs. *ARA&A*, 36:267–316, 1998.
- [14] M. Rauch, J. Miralda-Escude, W. L. W. Sargent, T. A. Barlow, D. H. Weinberg, L. Hernquist, N. Katz, R. Cen, and J. P. Ostriker. The Opacity of the Ly alpha Forest and Implications for Omega B and the Ionizing Background. *ApJ*, 489:7–+, November 1997.
- [15] Michael Rauch. *Lyman Alpha Forest*. Encyclopedia of Astronomy Astrophysics. Institute of Physics Publishing, 2006–902006.
- [16] C. C. Steidel, K. L. Adelberger, M. Giavalisco, M. Dickinson, and M. Pettini. Lyman-Break Galaxies at $z > 4$ and the Evolution of the Ultraviolet Luminosity Density at High Redshift. *ApJ*, 519:1–17, July 1999.
- [17] C. C. Steidel, K. L. Adelberger, A. E. Shapley, M. Pettini, M. Dickinson, and M. Giavalisco. Ly α Imaging of a Proto-Cluster Region at $\langle z \rangle = 3.09$. *ApJ*, 532:170–182, March 2000.
- [18] P. G. van Dokkum. Cosmic-Ray Rejection by Laplacian Edge Detection. *PASP*, 113:1420–1427, November 2001.
- [19] S. Veilleux, B. J. Weiner, D. S. N. Rupke, M. McDonald, C. Birk, J. Bland-Hawthorn, A. Dressler, T. Hare, D. Osip, C. Pietraszewski, and S. N. Vogel. MMTF: The Maryland-Magellan Tunable Filter. *AJ*, 139:145–157, January 2010.